The Astrophysical Journal, 768:196 (14pp), 2013 May 10 doi:10.1088/0004-637X/768/2/196

THE UV LUMINOSITY FUNCTION OF STAR-FORMING GALAXIES VIA DROPOUT SELECTION AT REDSHIFTS $z \sim 7$ AND 8 FROM THE 2012 ULTRA DEEP FIELD CAMPAIGN

Matthew A. Schenker[1], Brant E. Robertson[2], Richard S. Ellis[1], Yoshiaki Ono[3], Ross J. McLure[4], James S. Dunlop[4], Anton Koekemoer[5], Rebecca A. A. Bowler[4], Masami Ouchi[3], Emma Curtis-Lake[4], Alexander B. Rogers[4], Evan Schneider[2], Stephane Charlot[6], Daniel P. Stark[3], Steven R. Furlanetto[7], and Michele Cirasuolo[4]
[1] Department of Astrophysics, California Institute of Technology, MC 249-17, Pasadena, CA 91125, USA; schenker@astro.caltech.edu
[2] Department of Astronomy and Steward Observatory, University of Arizona, Tucson, AZ 85721, USA
[3] Institute for Cosmic Ray Research, University of Tokyo, Kashiwa City, Chiba 277-8582, Japan
[4] Institute for Astronomy, University of Edinburgh, Edinburgh EH9 3HJ, UK
[5] Space Telescope Science Institute, Baltimore, MD 21218, USA
[6] UPMC-CNRS, UMR7095, Institut d'Astrophysique de Paris, F-75014 Paris, France
[7] Department of Physics & Astronomy, University of California Los Angeles, Los Angeles, CA 90095, USA
Received 2013 January 7; accepted 2013 March 22; published 2013 April 26

ABSTRACT

We present a catalog of high-redshift star-forming galaxies selected to lie within the redshift range $z \simeq 7$–8 using the Ultra Deep Field 2012 (UDF12), the deepest near-infrared (near-IR) exposures yet taken with the *Hubble Space Telescope* (*HST*). As a result of the increased near-IR exposure time compared to previous *HST* imaging in this field, we probe ∼0.65 (0.25) mag fainter in absolute UV magnitude, at $z \sim 7$ (8), which increases confidence in a measurement of the faint end slope of the galaxy luminosity function. Through a 0.7 mag deeper limit in the key F105W filter that encompasses or lies just longward of the Lyman break, we also achieve a much-refined color–color selection that balances high redshift completeness and a low expected contamination fraction. We improve the number of dropout-selected UDF sources to 47 at $z \sim 7$ and 27 at $z \sim 8$. Incorporating brighter archival and ground-based samples, we measure the $z \simeq 7$ UV luminosity function to an absolute magnitude limit of $M_{\rm UV} = -17$ and find a faint end Schechter slope of $\alpha = -1.87^{+0.18}_{-0.17}$. Using a similar color–color selection at $z \simeq 8$ that takes our newly added imaging in the F140W filter into account, and incorporating archival data from the HIPPIES and BoRG campaigns, we provide a robust estimate of the faint end slope at $z \simeq 8$, $\alpha = -1.94^{+0.21}_{-0.24}$. We briefly discuss our results in the context of earlier work and that derived using the same UDF12 data but with an independent photometric redshift technique.

Key words: dark ages, reionization, first stars – galaxies: evolution – galaxies: formation

Online-only material: color figures

1. INTRODUCTION

Great progress has been made in recent years in studies of the population of star-forming galaxies at redshifts $z \simeq 7$–8. Following installation of the infrared Wide Field Camera 3 (WFC3) on the *Hubble Space Telescope* (*HST*), the number of candidates has risen from a few (Bouwens et al. 2008) to ≃100 (McLure et al. 2010; Bouwens et al. 2010; Oesch et al. 2010; Yan et al. 2010). In addition to providing hints of the early galaxy population to $z \simeq 8$, previous data sensitive to $z \sim 7$ galaxies have provided initial determinations of their rest-frame UV colors, stellar populations (McLure et al. 2011; Bouwens et al. 2012b; Dunlop et al. 2012), stellar masses and likely ages (Labbé et al. 2010; González et al. 2010; McLure et al. 2011; Finkelstein et al. 2012), and nebular emission line strengths (Labbe et al. 2012). Our work builds upon these previous efforts to present the first dropout-selected samples and luminosity function determinations for redshift $z \sim 7$ and $z \sim 8$ sources from the 2012 Hubble Ultra Deep Field project (hereafter UDF12; GO 12498, PI: R. Ellis).

Before UDF12, progress has naturally been greatest at redshift $z \simeq 7$ where synergy between ground- and space-based surveys has effectively exploited the full dynamic range of accessible galaxy luminosities. Early surveys from Subaru (Ouchi et al. 2009) and the ESO Very Large Telescope (Castellano et al. 2010) have probed the luminous component of the star-forming population over an area >1000 arcmin^2. More recently, the UltraVISTA survey has covered 3600 arcmin^2 in the COSMOS field, locating $z \simeq 7$ galaxies to $M_{\rm UV} = -22.7$ (Bowler et al. 2012).

However, only *HST* can probe the important faint end of the galaxy luminosity function at these redshifts. An early result from the 2009 Hubble Ultra Deep Field campaign (hereafter UDF09; GO 11563, PI: Illingworth) was the discovery of an abundant population of sub-luminous galaxies at $z \simeq 7$ (Oesch et al. 2010; Bunker et al. 2010; McLure et al. 2010) corresponding to a Schechter faint end slope α between −1.7 to −2.0. In such a distribution, the bulk of the integrated luminosity density arises from low luminosity galaxies that may be responsible for maintaining cosmic reionization (Robertson et al. 2010).

Clearly the luminosity function of star-forming galaxies at redshifts $z \simeq 7$–8 is of great importance. However, given the large range in luminosity that must be sampled, wider-field *HST* surveys have proved an important complement to panoramic ground-based surveys. WFC3 data from the GOODS Early Release Science (ERS; Windhorst et al. 2011) and the CANDELS fields (Grogin et al. 2011; Koekemoer et al. 2011) have sampled intermediate luminosities $-21 \lesssim M_{\rm UV} \lesssim -19$. The HIPPIES and BoRG pure parallel surveys have provided additional candidates at $z \sim 8$ (Yan et al. 2011; Trenti et al. 2011; Bradley et al. 2012).

Collectively these surveys have provided a reasonably clear view of the galaxy luminosity function at $z \simeq 7$ at the

luminous end but there remain disagreements regarding the precision with which the faint end slope is determined. While the UDF09 collaboration has measured a faint-end slope of $\alpha_{z\sim7} = -2.01 \pm 0.21$ (Bouwens et al. 2011) incorporating the UDF, parallel fields, and the ERS data, a competing determination utilizing the size-luminosity relation measured from the UDF09 data and the CANDELS Deep+Wide surveys in three fields finds a shallower faint-end slope of $\alpha_{z\sim7} = -1.7\pm0.1$ (Grazian et al. 2012). The luminosity function at $z \simeq 8$ is even more uncertain, both because of the limited depth of the necessary photometry (Dunlop et al. 2012) and the possibility of contamination from lower redshift sources.

Distant star-forming galaxies are commonly found using some variant of the Lyman break technique pioneered by Steidel et al. (1996). At $z \gtrsim 6.5$, the opacity due to neutral hydrogen in the intergalactic medium means the source flux below a rest-wavelength $\lambda_{\rm rest} = 1216$ Å is dimmed by factors $\geqslant$5 (Madau 1995). A search exploiting this effect has utilized one of two methods. In the "dropout" technique, objects are selected within a carefully chosen window in color–color space specifically tuned to select star-forming galaxies within the required redshift range while minimizing the contribution from lower redshift contaminants. At $z \sim 7$ (where the Lyman break falls near the overlap of the *HST* z_{850} and Y_{105} filters), the Lyman dropout is chosen via a red color in $z - Y$, and the star-forming nature of the galaxy via a blue color in $Y - J$. Additionally, candidates are required to lie below a certain threshold in deep optical data; this further limits contamination by lower redshift sources. Early demonstrations of the dropout technique at redshifts $z \gtrsim 6$ were presented by Bunker et al. (2004) and Bouwens et al. (2004).

An alternative approach uses the full array of broadband detections and upper limits in the context of photometric redshift codes (McLure et al. 2010, 2011; Finkelstein et al. 2010). These codes employ a range of synthetic spectra for galaxies (e.g., Bruzual & Charlot 2003) over all redshifts of interest and optimum fits are produced for each source in the catalog. As in the dropout selection technique, leverage comes primarily from the Lyman break but the method is particularly advantageous when detections are available in more than three filters.

In general, agreement between the two techniques is often quite good (McLure et al. 2011). However, the methods are distinct and each has aspects relevant for interpreting their photometric samples. The spectral energy distribution (SED) method provides redshift probability distributions for individual sources but may be susceptible to systematic errors inherent in population synthesis models, such as uncertainties in the reddening law and star-formation histories, when differentiating between low-redshift interlopers and true high-redshift sources. In contrast, our dropout selection utilizes the observed color information independent of stellar population synthesis modeling, but requires careful simulations to quantify the possible presence of low-redshift contaminants satisfying the break criterion. It also assumes that the intrinsic colors of possible contaminants do not differ at fainter luminosities. Given their complementary features, particularly for estimating contributions from contaminants, independent luminosity function determinations from both methods will be helpful in furthering progress. The goal of the present paper is therefore to exploit this unique data to provide the best current constraints on the UV luminosity function of star-forming galaxies at redshift 7 and 8 using the dropout technique. A companion UDF12 paper (McLure et al. 2013) presents the results of a search through the data for $z \geqslant 6.5$ candidates using the photometric redshift technique.

The present paper is one in a series devoted to scientific results from the UDF12 campaign, which provides a significant advance over the earlier UDF09 imaging in this field appropriate for the present luminosity function study and the complementary analysis discussed in McLure et al. (2013). The UDF12 survey design and its data processing are discussed in Koekemoer et al. (2013). Public versions of the final reduced WFC3/IR UDF12 images, incorporating all earlier UDF data, are available to the community on the UDF12 website.[8] Initial $z \geqslant 8.5$ detections in the UDF12 data were presented by Ellis et al. (2013), while the UV continua of high-redshift candidates were measured by Dunlop et al. (2013). A review of the implications of the survey in the context of cosmic reionization including the results of the present paper is provided in Robertson et al. (2013).

A plan of the paper follows. In Section 2, we introduce the UDF12 data and the brighter ground-based and *HST* data sets and their reductions essential for realizing an analysis of the luminosity function at $z \simeq 7$ and 8. Section 3 discusses the important decisions we have taken in color–color space to optimize the completeness of galaxies at these redshifts, while minimizing contamination from lower redshift sources. Section 3 also presents the final list of galaxies in the two redshift intervals that we use for our analysis. In Section 4, we present our luminosity functions and in Section 5 we briefly discuss our results in the context of earlier work, highlighting the important advances made possible through the UDF12 campaign.

Throughout this paper, we adopt a Λ-dominated, flat universe with $\Omega_\Lambda = 0.7$, $\Omega_M = 0.3$, and $H_0 = 70\,h_{70}\,{\rm km\,s^{-1}\,Mpc^{-1}}$. All magnitudes in this paper are quoted in the AB system (Oke & Gunn 1983). We will refer to the *HST* Advanced Camera for Surveys (ACS) and WFC3/IR filters F435W, F600LP, F606W, F775W, F814W, F850LP, F098M, F105W, F125W, F140W, and F160W as B_{435}, V_{600}, V_{606}, i_{775}, i_{814}, z_{850}, Y_{098}, Y_{105}, J_{125}, J_{140}, and H_{160}, respectively.

2. DATA

Central to any analysis of the galaxy luminosity function is the collation of a complete sample of galaxies within the chosen redshift interval spanning a wide range in luminosities, free from bias and with any interlopers minimized. In this section, we introduce the UDF12 and more luminous auxiliary data sets.

2.1. UDF

To provide the best constraints on the faint end of the luminosity function at $z \simeq 7$ and 8, the primary advance of this paper is the increased depth and redshift fidelity provided by our new UDF12 survey. The UDF12 program data set (described in full in Koekemoer et al. 2013) represents a significant improvement over the previous UDF09 observations in several respects. In particular, the survey was purposefully designed to improve our understanding of the redshift $z \simeq 7$ and 8 luminosity functions. First, we increased the total exposure time in the key Y_{105} filter over that in the UDF09 campaign by a factor of four, with the addition of 71 new orbits. As the Lyman break lies near the edge of the filter transmission profile for galaxies at $z \simeq 7$, this ensures we can probe significantly fainter (by $\simeq$0.4 mag) in absolute magnitude at $z \simeq 7$ and with considerably greater fidelity in redshift selection at $z \simeq 8$ (Ellis et al. 2013). A further improvement is the addition of comparable imaging in the newly utilized J_{140} filter. By stacking our detections in

[8] http://udf12.arizona.edu/

Table 1
Data Sets, Candidates, and Survey Depth 5σ AB

Name	Area (arcmin^2)	$z \sim 7$ Candidates	$z \sim 8$ Candidates	Y_{105W}	J_{125W}	J_{140W}	H_{160W}
UDF12	4.6	47	27	30.0	29.5	29.5	29.5
UDF-P1	4.6	15	10	28.9	29.0	···	28.7
UDF-P2	4.6	13	10	29.0	29.2	···	28.7
ERS	36.8	15	4	27.6[a]	28.0	···	27.5
CANDELS-Deep	64.9	32	18	28.2	28.1	···	27.7

Note. [a] The ERS program replaces the Y_{105} filter with the Y_{098} filter.

this filter with either those at J_{125} at $z \simeq 7$ or H_{160} at $z \simeq 8$, we secure improved detections that correspond to extending the depth by an additional $\simeq$0.1 mag in each case.

Our final analysis is based on the compilation discussed by Koekemoer et al. (2013) which incorporates all earlier WFC3 imaging in the UDF including the earlier UDF09 campaign (GO 11563; PI: Illingworth) and less deep imaging undertaken as part of the CANDELS survey (GO 12060; PIs: Faber & Ferguson). In total, the imaging constitutes 100, 39, 30, and 84 orbits in each of the Y_{105}, J_{125}, J_{140} and H_{160} filters, respectively (see Koekemoer et al. 2013 for further details). An important associated data set in this field is the ultra deep ACS imaging data from the 2004 UDF campaign (Beckwith et al. 2006), which is essential for a further rejection of low redshift sources.

2.2. Auxiliary Data

To constrain the bright end of the $z \simeq 7$ and 8 luminosity functions, we take advantage of several auxiliary WFC3 data sets that are somewhat shallower than our UDF12 data but nonetheless unique in their coverage and depth. At $z \simeq 7$, we include the UDF parallel fields, UDF-P1 and P2 (sometimes referred to as UDF-P12 and P34, respectively) from various surveys including UDF05 (GO 10532, PI: Stiavelli) and the aforementioned UDF09 survey, the Early Release Science (ERS) WFC3 campaign from the WFC3 Science Team (GO 11359, PI: O'Connell; Windhorst et al. 2011), and imaging in the GOODS-S field from CANDELS-Deep (Grogin et al. 2011; Koekemoer et al. 2011). We also adopt the data points from the ground-based surveys of Ouchi et al. (2009), Castellano et al. (2010), and Bowler et al. (2012), which provide vital observations of the rare population of galaxies brighter than $M_{\mathrm{UV},\star}$.

At $z \sim 8$, it is difficult for ground-based programs to provide any meaningful constraints, so we instead include data provided by two *HST* pure-parallel WFC3 programs: HIPPIES (GO/PAR 11702, PI: Yan; Yan et al. 2011) and BoRG (GO/PAR 11700, PI: Trenti; Trenti et al. 2011; Bradley et al. 2012). As the shortest wavelength coverage of these surveys is provided only with the V_{606W} (or V_{600LP}), Y_{098}, and J_{125} filters, a robust spectral break can only be verified between Y_{098} and J_{125}, as the wavelength spanned between V_{606W} and Y_{098} is too great and there remains no optical rejection filter at shorter wavelengths. Thus, these fields can only usefully identify galaxies at $z \sim 8$, and therefore we do not use them for our selection at $z \sim 7$.

We summarize the filter coverage, survey area, limiting depths in the selection filter(s), and the number of high redshift candidates for each of these auxiliary data sets in Table 1.

2.3. Data Reduction

Prior to applying photometric color cuts optimized for the selection of $z \simeq 7$ and 8 galaxies, each survey data was similarly reduced to provide a series of processed and calibrated WFC3 frames. We describe below the data reduction steps taken for each field.

2.3.1. UDF and Parallels

The preliminary processing stages that yield images ready for source selection are discussed in detail by Koekemoer et al. (2013). Briefly, we first process the raw images using the Pyraf/STDAS task *calwf3*, which flags bad pixels and corrects for bias and dark current throughout the detector. After processing, the images are then registered and stacked using a version of the MultiDrizzle algorithm (Koekemoer et al. 2003) to create the final mosaics on a pixel scale of 0.″03 per pixel. This processing was carried out to create reductions of the UDF, UDF-P1, and UDF-P2 fields.

2.3.2. ERS and CANDELS-Deep

For the ACS data in the CANDELS-Deep and ERS fields, we use the publicly available v2.0 mosaics from the GOODS campaign (Giavalisco et al. 2004). We augment this with our own compilations of both the i_{814} and z_{850} data taken in parallel during the CANDELS WFC3 campaign. We combine the publicly available single epoch mosaics for these filters, weighting by exposure time, using the image combination routine SWARP (Bertin et al. 2002). In the case of the z_{850} data, we add this to the already existing GOODS mosaic.

We combine the public WFC3 mosaics from the CANDELS team (Koekemoer et al. 2011) in the same manner across CANDELS-Deep. For the ERS WFC3 data, we use the reduction described in McLure et al. (2011). Due to the lack of subpixel dithering available in the wider area fields, the CANDELS and ERS mosaics were produced with final pixel scales of 0.″06 per pixel.

2.3.3. BoRG + HIPPIES

As the BoRG and HIPPIES programs are pure parallel surveys, their data products differ significantly in many ways from those discussed above. Details of the relevant observation strategies can be found in Trenti et al. (2011) and Bradley et al. (2012). The initial data set presented in Bradley et al. (2012) consists of 59 independent fields with an output pixel scale of 0.″08 per pixel and a median 5σ depth of 27.5 in J_{125} which varies significantly from field to field.

We have analyzed the updated BoRG data set which includes a further 10 currently unpublished fields. The details of our reduction will be described in R. A. A. Bowler et al. (2013, in preparation). We encountered significant difficulties in compiling a robust list of candidates. Although we assembled a final list of 48 candidate high-redshift objects, we cannot apply the same rigorous constraints in ensuring each is not an artifact or Galactic star due to the coarser pixel scale and absence of a

dithered observing strategy. Such limitations are inherent in the use of the pure parallel observing mode.

Recognizing the unfortunate loss of valuable additional data, we did explore the issue of potential contamination from stellar sources via a simulation to determine how robustly we could rule out unresolved objects based solely upon the BoRG point-spread function (PSF). We created a galaxy template with a physical half-light radius of 0.″10, chosen to match the median found for the luminous ($0.3 < L/L_{\star,z=3} < 1.0$) $z \sim 8$ UDF12 galaxies analyzed in Ono et al. (2012). This template was then convolved with the measured PSF and inserted into the images, along with unresolved point sources, at steps of 0.1 in magnitude. Observed half-light radii of all inserted sources were then re-measured with SExtractor. We found that the 95% confidence intervals of our synthetic galaxies and genuine point sources already begin to overlap at a detection significance of $\sim 24\sigma$ in the J_{125} filter (equivalent to an object with $J_{125} = 25.8$ for the median depth of the survey). Thus at quite bright luminosities at $z \simeq 8$, it is very difficult to robustly exclude point sources. Ultimately, at the 5σ limit, the observed median half-light radii of point sources and synthetic galaxies differ by only 0.3 pixels, rendering discrimination impossible.

In view of these challenges, we chose not to include our analysis of the up-to-date BoRG data in our determination of the $z \sim 8$ luminosity function, other than the inclusion of the data points of Bradley et al. (2012). In Section 4, we note the effect of excluding this subset of data.

2.4. Photometry

In the case of the UDF12, which pushes *HST* to new limiting depths, we adopted a robust technique to locate and measure the fluxes from each faint source, rather than relying on errors output from the SExtractor source extraction code (Casertano et al. 2000). As the correlated noise produced as a result of applying the MultiDrizzle algorithm produces a subtle underestimate of uncertainties when using SExtractor, in the specific case of the UDF12 we chose to use our own IDL photometry routine to compute all fluxes quoted in this paper.

We briefly summarize the various stages. Processing proceeds by using a χ^2 stack of all the images to identify regions of blank sky over the area in question. A grid of blank apertures is then generated, with separation larger than the `pixfrac` footprint of MultiDrizzle, ensuring that noise between adjacent apertures is not correlated. To estimate the level of any residual background around an object of interest, we take the median flux of the 50 closest blank apertures. We adopt the root mean square of the flux in these blank apertures as our uncertainty in the background level. Fluxes are then computed using the APER routine in IDL (Landsman 1993). For the shallower non-UDF12 fields, although we utilized SExtractor to compute fluxes and background levels, the flux uncertainties were still estimated using this improved technique.

As the *HST* PSF varies significantly with wavelength (particularly between the ACS optical images and near-infrared images from WFC3), it is important to account for this change when measuring accurate colors. To improve detections and color measurements for the faintest sources, aperture sizes should be quite small yet properly account for wavelength-dependent PSF variations. We chose circular apertures whose diameters encircle $\geqslant$70% of the total flux from a point source. For the ACS B_{435}, V_{606}, i_{775}, i_{814}, and z_{850} filters, we adopt aperture diameters of 0.″30 in all fields processed with 0.″03 pixel diameter (UDF12, UDF-P1, and UDF-P2), and 0.″40 in all other fields. For the WFC3 filters, the aperture diameters are 0.″40, 0.″44, 0.″47, and 0.″50, for Y_{105}/Y_{098}, J_{125}, J_{140}, and H_{160}, respectively. Such small apertures remain meaningful both because of the FWHM of the *HST* PSF (ranging from 0.″09 in B_{435} to 0.″17 in H_{160}), and the precise degree of alignment of the individual image sub-exposures (better the 0.″005 in the UDF; Koekemoer et al. 2013). In a related paper, Ono et al. (2013) validate these choices by measuring half-light radii, r_{hl}, for stacks of our high-redshift samples, and find values of 0.36 kpc at both $z \sim 7$ and 8, which translate to angular half-light radii of 0.″07 (not including any broadening due to the PSF). To correct to total magnitudes for the purpose of computing the luminosity function, we apply an aperture correction of 0.47 mag, determined by measuring the flux of a synthetic galaxy template with this half-light radius that falls outside our apertures.

3. CANDIDATE SELECTION

We now turn to the photometric selection of star-forming galaxies at $z \simeq 7$ and 8, using the photometric catalogs generated as discussed in Section 2. A key issue for our dropout selection technique is the optimum choice of the two color cuts used to select candidates. The goal is to balance completeness in high-z selection against a low fraction of foreground interlopers and spurious sources. As the available filter sets differ for each of the component surveys, we discuss each case in turn.

3.1. Potential Contaminants

A selection criterion tuned to select only high-redshift galaxies at high confidence, with essentially no contamination, would be impractical, leading to a severely limited sample. In order to be inclusive in such a search, a crucial condition for an accurate determination of the luminosity function, a small degree of contamination can be tolerated provided the fraction is reasonably well-understood.

In fact, the primary sources of contamination in high-redshift searches are now well-known. We briefly review them here. Low-temperature Galactic dwarf stars display quite similar colors to high redshift galaxies in the near-infrared (e.g., Bowler et al. 2012). While ground-based surveys can only constrain stellar contamination by comparing SEDs of cool stars to observed colors (Bowler et al. 2012), WFC3 data has the distinct advantage of an extremely sharp PSF, ranging from 0.″15 in Y_{105} to 0.″18 in H_{160}. Previous studies in the UDF have utilized this to conclude that Galactic stars are not expected to contribute significantly (<2%) to contamination in extremely deep, small area surveys (Finkelstein et al. 2010; Bouwens et al. 2011).

We have also investigated our ability to rule out unresolved contaminants with our UDF12 data. We conducted a simulation similar to that described in Section 2.3.3, inserting both point sources and simulated galaxies into the image and recovering their observed half-light radii distributions as a function of magnitude. In this case, we used a galaxy model with an intrinsic half-light radius of only 0.″07 to match the value found for stacks of the faintest UDF12 galaxies in Ono et al. (2012). This template was then convolved with the observed PSF before insertion into the image. In this case, we found that the 95% confidence intervals of the point sources and our galaxy model did not overlap until $m = 28.6$. Brightward of this magnitude, none of the 19 high-redshift sources selected in this study show half-light radii consistent with a point source at the 2σ level, further reinforcing our conclusion that stellar contamination should not be significant.

A more relevant concern is potential interlopers at $z \sim 2$. Around this redshift, the Balmer and 4000 Å breaks will lie near the same observed wavelengths where we search for a Lyman break in our high-redshift sources. However, unlike the Lyman break, the Balmer break has a maximum possible depth, aiding us in isolating robust high-redshift sources (see Figure 2 of Kriek et al. 2010 for actual measurements at $z > 0.5$). Due to our extraordinarily deep optical data, these objects must either then be severely reddened in the rest-frame ultraviolet or significantly affected by photometric scatter in order to be picked up by our selection criteria. However, we recognize that there may be the potential for some contamination from rare sources with extreme emission line equivalent widths (e.g., Taniguchi et al. 2010; Atek et al. 2011; Brammer et al. 2013) or with other sharp spectral features that can mimic the presence of a Lyman break (Hayes et al. 2012). The possible effects of both types of contaminants are discussed further in the context of our contamination simulations (Section 3.3).

3.2. Optical Non-detection Criteria

Applying a rigorous set of optical non-detection criteria is key to obtaining a clean sample of high-redshift sources by removing the lower redshift contaminants we describe above, as we expect all intrinsic flux from true high-redshift sources to be nearly extinguished by neutral Hydrogen at these wavelengths (Madau 1995). Here we adopt a slightly modified version of the criteria used in Bouwens et al. (2011) to eliminate sources with marginal optical detections from our selections.

The criteria we apply are as follows. (1) The measured flux in each filter shortward of the dropout filter is less than 2.0σ. For the z-drops, this includes B_{435}, V_{606}, and i_{775}; for the Y-drops, we add z_{850}. (2) No more than one of the filters listed above shows a detection above 1.5σ. (3) To effectively add all the optical data, we finally require that $\chi^2_{\rm opt}$ [9] must be less than a threshold value, depending on the observed magnitude of the source. We compute this value using both our standard 0.″30 diameter circular apertures, and a smaller 0.″21 aperture, to rule out the most compact contaminants. At or below the 5σ limit of $m_{\rm AB} = 29.5$ (in uncorrected, aperture magnitudes), we adopt a $\chi^2_{\rm opt}$ upper limit of 2.5, while at the 10σ limit of $m_{\rm AB} = 28.7$ we relax this to limit 5.0. A linear interpolation is used to determine the limit for magnitudes between the 5σ and 10σ level.

3.3. Contamination Simulations and the Adopted UDF12 Color–Color Selection

To estimate the number of contaminants we expect, we utilized the excellent *HST* photometry for objects at $25.0 < H_{160} < 27.0$ (as measured in our 0.″5 diameter apertures) in the UDF. As we can robustly rule out the presence of a Balmer break at this depth, we selected as our base color distribution of contaminants all sources in this magnitude range that displayed at least one optical detection. The key assumption in our simulations is that the color distribution of these potential contaminants is unchanged as one moves down to the fainter magnitudes where the majority of our dropout galaxies lie. If the relative number of strong emission line galaxies which mimic sharp spectral breaks (e.g., Atek et al. 2011) increases significantly toward faint magnitudes, then our assumption may fail. However, such sources are surely rare and considering the color trend in this magnitude range, we see no evidence of such an effect. For our sample at $25.00 < H_{160} < 25.25$, the median $z_{850} - Y_{105}$, $Y_{105} - J_{125}$, and $J_{125} - H_{160}$ colors are 0.45, 0.31, and 0.31, respectively. At $26.75 < H_{160} < 27.00$, these three colors show even less extreme median colors of 0.32, 0.17, and 0.15.

We then create an array of synthetic sources, matched to the actual number of observed sources in the UDF in bins of 0.1 mag. To get an accurate representation of sources intrinsically below our detection limit that have some chance of being scattered upward into detection, we extrapolate the number counts beyond $H_{160} = 28.7$ (equivalent to a source at 10.0σ) as a function of magnitude via a power law down to sources intrinsically as faint as 1.0σ. The colors of these synthetic sources are chosen to obey the same color distribution as the brighter contaminant population described above, but noise consistent with their synthetic magnitudes is then added. These sources are then subject to the same optical non-detection criteria described above, but the colors cuts in $z_{850} - Y_{105}$ and $Y_{105} - J_{125}$ ($Y_{105} - J_{125}$ and $J_{125} - H_{160}$) for z-drops (Y-drops) are varied in steps of 0.05, as shown in Figure 1. To create these plots, we repeated the simulations for $N = 1000$ UDF fields.

Clearly, the most robust constraint on eliminating contaminants comes from requiring a large break in the bluer color for each sample, but gains are also made by limiting the color longward of the break to relatively blue values. Provided with these estimates, we chose to implement the color selection criteria as shown in Figure 1:

$$z_{850} - Y_{105} > 0.7, \quad (1)$$

$$Y_{105} - J_{125} < 0.4. \quad (2)$$

At $z \sim 8$, we use

$$Y_{105} - J_{125} > 0.5, \quad (3)$$

$$J_{125} - H_{160} < 0.4. \quad (4)$$

This leads to a selection for z-drops broadly within the redshift range $6.2 < z < 7.3$. For the $z \simeq 8$ study, we use our new ultra-deep WFC3 Y_{105} as the dropout filter, which leads to a sample spanning the redshift range $7.3 < z < 8.5$. A discussion of more distant sources in the UDF is provided by Ellis et al. (2013).

Finally, to ensure our sources are robust, we demand a detection significance of 3.5σ in the filter immediately longward of the Lyman break (Y_{105} for our z-drops, J_{125} for our Y-drops), and a similarly robust detection in one further WFC3 filter at longer wavelengths.

These selection criteria are designed to provide as large a sample of galaxies as possible above redshift 6.5, while minimizing the effect of contamination. We plot selection functions for both z-drops and Y-drops in Figure 2 (see Section 4.1 for details on the selection function simulation). At bright magnitudes $J_{140} < 27.5$, our z-drop color cuts provide a nearly complete census of star-forming galaxies between $6.30 < z < 7.15$, while the Y-drop cuts do the same between $7.35 < z < 8.60$.

Due to our strict criterion for optical non-detection and the area subtended by other sources in UDF12, our maximum selection efficiency does not exceed ∼65%. For both our z- and Y-drop selections, 22% of the area is excluded due to objects occupying the image. For the more luminous z-drops, a further 13% of the area is excluded due to our optical exclusion criteria. As we impose more stringent criteria on the fainter sources, our

[9] Defined as $\chi^2_{\rm opt} = \Sigma_i \,{\rm sign}(f_i)(f_i/\sigma_i)^2$, where the i index runs across B_{435}, V_{606}, and i_{775} for z-drops; additionally i_{814} where available, and z_{850} for Y-drops.

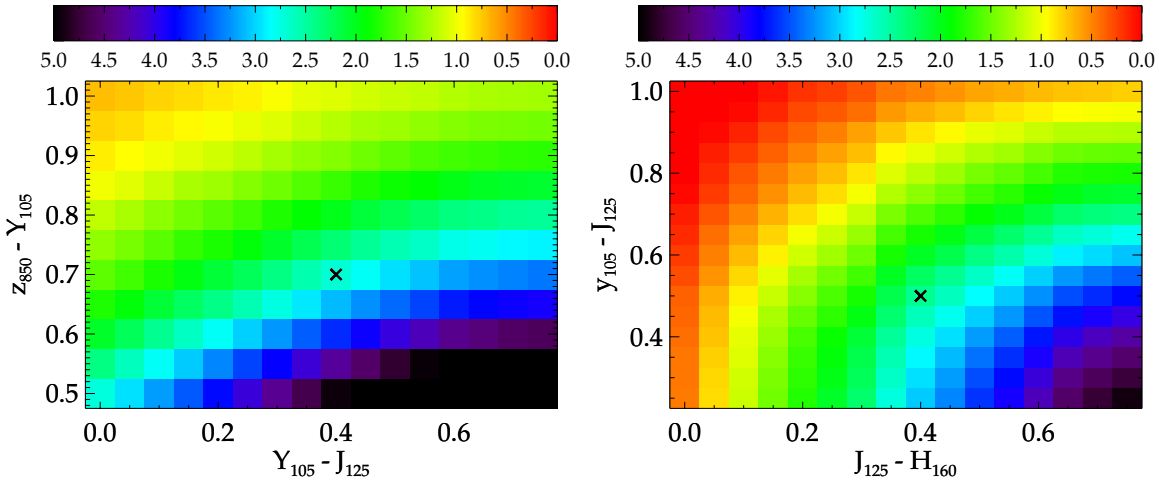

Figure 1. Left: number of z_{850}-drop contaminants per UDF12 field as a function of the color cuts in $z_{850} - Y_{105}$ and $Y_{105} - J_{125}$. We assume that these contaminants obey the same intrinsic color distribution as UDF12 objects with $25.0 < H_{160} < 27.0$, as described in Section 3.3. The selection criteria are defined such that the $z_{850} - Y_{105}$ must be greater than the value on the y-axis to be selected, and the $Y_{105} - J_{125}$ less than the value on the x-axis. Right: as left, but for Y_{105}-drops. Our chosen cuts are marked by the black "×" in each figure. We refer the reader to Figure 3 for a visualization of our final cuts.

(A color version of this figure is available in the online journal.)

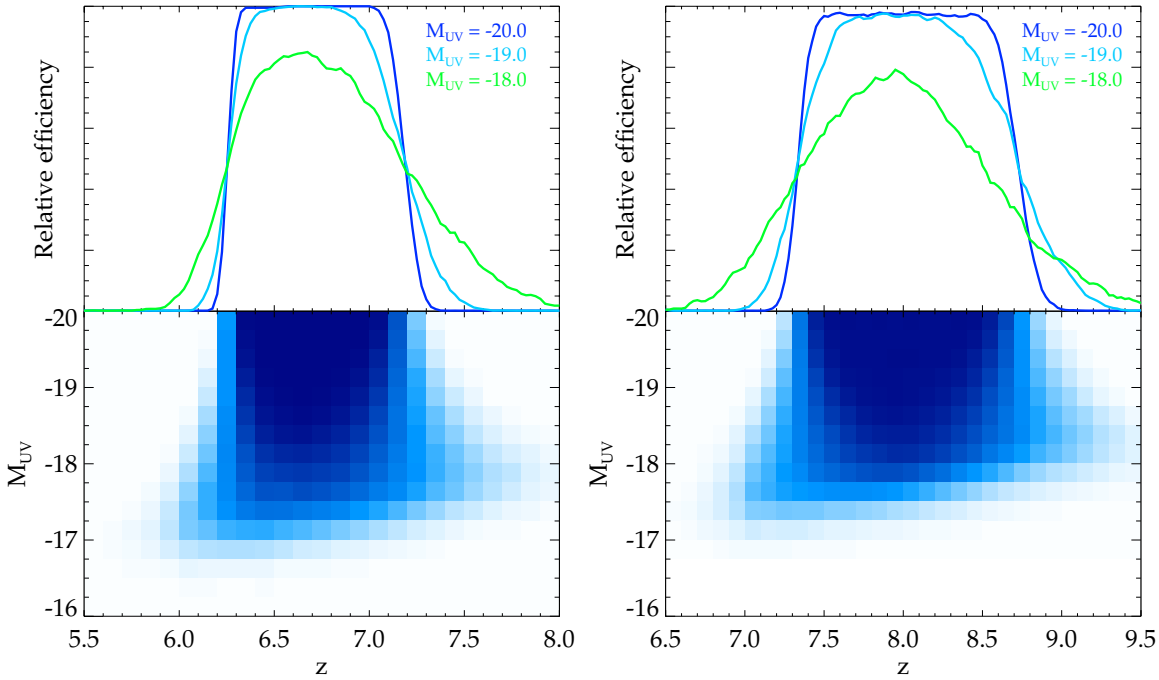

Figure 2. Left: selection function for z_{850}-drop galaxies in the UDF, as a function of $M_{\rm UV}$ and redshift, constructed using the simulations discussed in Section 4.1. We have assumed that these galaxies display no Lyα in emission. Even at bright magnitudes, maximum efficiency is only ∼0.65 due to the area subtended by other objects and our strict optical non-detection criteria, which result in a small fraction of true high-redshift sources being excluded. Right: equivalent selection function for Y_{105}-drops.

(A color version of this figure is available in the online journal.)

optical criteria reject 21% of the areal coverage for our $z \sim 7$ search. For our $z \sim 8$ search criteria, the optical exclusion criteria reject 16% of the area at the bright end and 24% at the faint end.

Extending our $Y_{105} - J_{125}$ color cut for z-drops to 0.5 would only add an extra ∼0.1 in redshift space to our selection function, as the color tracks are rapidly departing from our selection window as can be seen in Figure 3. This would additionally add an extra 0.3 expected contaminants. Combined with the concern that our new Y_{105} data is actually deeper than the existing z_{850} data, and that the primary contaminants themselves are intrinsically red, we opted for this conservative $Y_{105} - J_{125}$ color cut for our z-drop sample. Similarly, adding an extra 0.1 mag to our $J_{125} - H_{160}$ limit for Y-drops is expected to add ∼0.4 contaminants. As can be seen from the Y-drop color–color plot in Figure 3, the density of Y-drops with $J_{125} - H_{160}$ colors this red is quite low, so we chose to truncate the selection at $J_{125} - H_{160} < 0.4$, to limit the contamination. Adopting these cuts and all of our previously discussed selection criteria, we expect 2.79 and 1.42 contaminants per UDF field for z-drops and Y-drops, respectively.

We include candidate lists and photometry for our final selection of z-drops and Y-drops in Tables 2 and 3, respectively, and color–color plots in Figure 3. In total, we select 47

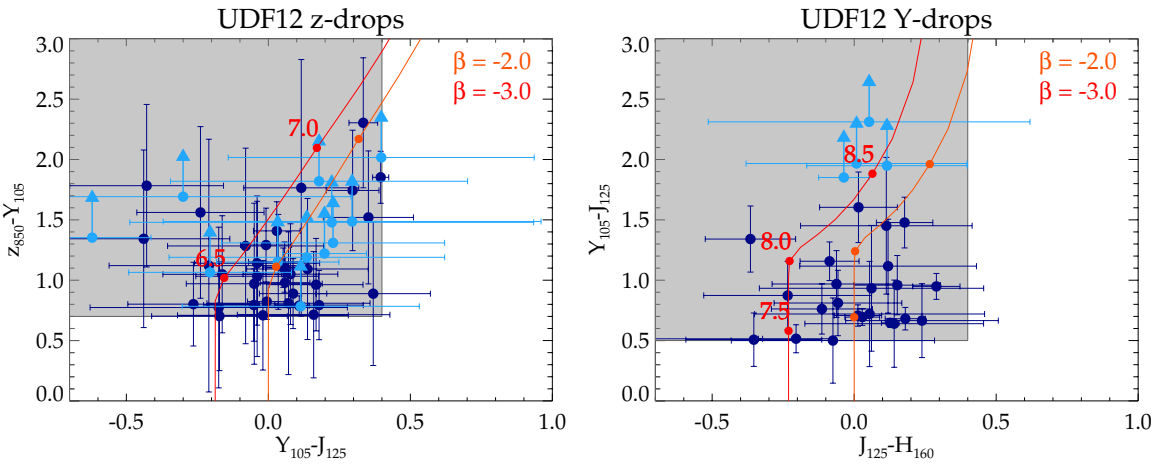

Figure 3. Color–color diagram of galaxies selected as z_{850}-drops (left) and Y_{105}-drops (right). The red and orange curves show the tracks of synthetic high-redshift galaxies for various UV continuum slopes β. The light blue points denote 1σ upper limits.

(A color version of this figure is available in the online journal.)

z-drops and 27 Y-drops, 20 and 9 of which were only identified using our new UDF12 data. The vast majority consist of single components in the WFC3 imaging. We detect a single Y-drop with two components separated at only 0.″4, UDF12-3764-6015. The aperture photometry of the main component is 1.2 mag brighter than the secondary component, and the two are considered as a single object in our later luminosity function analysis.

There are an additional four closely spaced pairs in our sample. We detect one pair of z-drops, UDF12-3983-6189 and UDF12-3989-6189, separated by only 0.″8. There are two additional pairs of Y-drops, UDF12-4474-6450 and UDF12-4470-6443, separated by 0.″9, and UDF12-4314-6285 and UDF12-4309-6277, separated by 1.″0. This second pair is also part of a larger association of Y-drops in our sample, consisting of 5 candidates all within a separation of <9.″0 (or 44 kpc at $z \sim 8$).

The final pair consists of a z-drop, UDF12-4036-8022, and a Y-drop, UDF12-4033-8026, so it is unlikely that these are physically related. Placing 47 z-drops and 27 Y-drops in the UDF at random, we find a z-drop/Y-drop pair at $d < 1.''0$ 23% of the time, so such serendipitous alignment is not unreasonable. The significant difference in photometry (and thus photometric redshift) supports this case: UDF12-4036-8022 has $Y_{105} - J_{125} = 0.0$, while UDF12-4033-8026 shows $Y_{105} - J_{125} = 0.9$.

3.4. UDF-P1 and UDF-P2

The two UDF parallel fields, observed as part of the UDF05 (GO 10632; PI: Stiavelli) and UDF09 (GO 11563; PI: Illingworth) campaigns, comprise the two data sets most similar to our UDF12 data set, though the depths are ∼0.5 mag shallower. As such, we utilize the same color–color criteria determined for our UDF12 selections. Because the optical data is shallower, we tighten our $\chi^2_{\rm opt}$ upper limit for selection to 1.5 (3.0) at the 5σ (10σ) aperture magnitude limit in each field. We utilize the ultra deep 128 orbit z_{814} ACS data taken in parallel to our main UDF12 program, which covers roughly 70% of the P2 WFC3/IR field. For z-drops within this area we impose an additional criterion of $z_{814} - Y_{105} > 2.0$ or $f_{814}/\sigma_{814} < 2.0$. This extra cut reinforces the requirement for a sharp spectral break and more fully utilizes our deep i_{814} data over the P2 field. From our synthetic spectral models at $z = 6.2$, where our selection function begins to yield sources, we expect an $i_{814} - Y_{105}$ color of 2.0, which increases further with increasing redshift. The $f_{814}/\sigma_{814} < 2.0$ criterion allows sources to pass our cuts in the case where the candidate is too faint to robustly establish a 2 mag break between i_{814} and Y_{105}. In practice, this only occurs in the CANDELS field (described below), but we consider it advantageous to keep uniform selection criteria where possible.

3.5. ERS

For the ERS data set, the Y_{098} filter was utilized, so we take care to alter our selection criteria accordingly. We chose to use the criteria derived by Bouwens et al. (2011) at $z \sim 7$, which, despite the different filter selection, produce a selection function that probes a similar range in redshift. These criteria are (1) $z_{850} - J_{125} > 0.9$, (2) $z_{850} - J_{125} > 0.8 + 1.1(J_{125} - H_{160})$, and (3) $z_{850} - J_{125} > 0.4 + 1.1(Y_{098} - J_{125})$. At $z \sim 8$, we adopt the Bouwens et al. (2011) $Y_{098} - J_{125}$ lower limit of 1.25, but choose the same $J_{125} - H_{160} < 0.4$ cut we use for the UDF fields, to ensure the selection functions for our analysis are as homogeneous as possible.

3.6. CANDELS

For the CANDELS field, we use the same criteria as adopted for UDF-P34, including the addition of the z_{814} criteria. Due to the varying depth of the data, we divide the CANDELS field into three distinct subregions when performing our analysis. The first region consists of the immediate area around the HUDF that is covered by ACS optical imaging taken as part of the HUDF04 (Beckwith et al. 2006) campaign, but falls outside the region probed by our UDF12 campaign, due to the smaller field of view of the WFC3 instrument. Here, the optical data is nearly a full 2 mag deeper than the available IR data, resulting in negligible contamination rates in our sample.

The remaining sample is further divided into an East and West region. The East and West regions have identical depth in the ACS data from the GOODS program and in the J_{125} and H_{160} filters, but the Y_{105} depth in the West region is approximately 0.4 mag shallower than that of the East. For the purposes of contamination and completeness simulations, we separate these two fields in order to properly account for the variation in depth.

Table 2
z-drops $6.2 < z < 7.3$

ID	R.A.	Decl.	z_{850LP}	Y_{105W}	J_{125W}	J_{140W}	H_{160W}	References
UDF12-3746-6328	3:32:37.46	−27:46:32.8	28.4 ± 0.1	27.6 ± 0.1[a]	27.5 ± 0.1[a]	27.4 ± 0.1[a]	27.3 ± 0.1[a]	1,3,9
UDF12-4256-7314	3:32:42.56	−27:47:31.4	30.4 ± 0.7	28.1 ± 0.1[a]	27.8 ± 0.1[a]	27.8 ± 0.1[a]	27.7 ± 0.1[a]	1,2,3,4,5,7,10
UDF12-4219-6278	3:32:42.19	−27:46:27.8	29.2 ± 0.2	28.1 ± 0.1[a]	28.1 ± 0.1	28.0 ± 0.1	28.1 ± 0.1[a]	1,3,4,7,9,10
UDF12-3677-7536	3:32:36.77	−27:47:53.6	29.0 ± 0.2	28.2 ± 0.1[a]	28.2 ± 0.1	28.3 ± 0.1	28.2 ± 0.1[a]	1,2,3,4,7,9,10
UDF12-3744-6513	3:32:37.44	−27:46:51.3	29.5 ± 0.2	28.4 ± 0.1[a]	28.3 ± 0.1	28.5 ± 0.1	28.5 ± 0.1	1,2,3,4,5,7,9,10
UDF12-4105-7156	3:32:41.05	−27:47:15.6	30.4 ± 0.7	28.7 ± 0.1	28.4 ± 0.1	28.3 ± 0.1	28.4 ± 0.1	1,2,3,5,10
UDF12-3958-6565	3:32:39.58	−27:46:56.5	29.8 ± 0.3	28.4 ± 0.1[a]	28.4 ± 0.1	28.4 ± 0.1	28.4 ± 0.1	1,2,3,5,7,9,10
UDF12-3638-7162	3:32:36.38	−27:47:16.2	29.5 ± 0.2	28.5 ± 0.1[a]	28.5 ± 0.1	28.4 ± 0.1	28.5 ± 0.1	1,2,3,4,5,7,9,10
UDF12-4057-6436	3:32:40.57	−27:46:43.6	29.9 ± 0.4	28.6 ± 0.1	28.6 ± 0.1	28.5 ± 0.1	28.7 ± 0.1	1,2,3,4,5,7,9,10
UDF12-4431-6452	3:32:44.31	−27:46:45.2	29.6 ± 0.3	28.7 ± 0.1	28.6 ± 0.1	28.7 ± 0.1	28.9 ± 0.2	1,7,9,10
UDF12-4160-7045	3:32:41.60	−27:47:04.5	30.0 ± 0.5	28.8 ± 0.1	28.8 ± 0.1	28.7 ± 0.1	28.8 ± 0.1	7,9,10
UDF12-4268-7073	3:32:42.68	−27:47:07.3	29.9 ± 0.3	29.1 ± 0.1	28.9 ± 0.1	28.9 ± 0.2	28.9 ± 0.1	10
UDF12-3313-6545	3:32:33.13	−27:46:54.5	<31.3	29.3 ± 0.1	28.9 ± 0.1	28.6 ± 0.1	29.0 ± 0.1	1,6,7,9,10
UDF12-3402-6504	3:32:34.02	−27:46:50.4	30.8 ± 0.7	29.3 ± 0.1	28.9 ± 0.1	29.0 ± 0.1	29.2 ± 0.2	7,10
UDF12-4182-6112	3:32:41.82	−27:46:11.2	30.3 ± 0.5	29.3 ± 0.1	29.1 ± 0.1	29.0 ± 0.1	28.9 ± 0.1	3,4,5,7,9,10
UDF12-3734-7192	3:32:37.34	−27:47:19.2	30.3 ± 0.5	29.3 ± 0.1	29.2 ± 0.2	29.5 ± 0.2	29.5 ± 0.2	10
UDF12-4239-6243	3:32:42.39	−27:46:24.3	30.0 ± 0.3	29.2 ± 0.1	29.3 ± 0.2	28.9 ± 0.1	29.1 ± 0.2	3,5,7,11
UDF12-3989-6189	3:32:39.89	−27:46:18.9	30.5 ± 0.8	29.4 ± 0.1	29.3 ± 0.2	29.5 ± 0.2	29.5 ± 0.2	1,10
UDF12-4068-6498	3:32:40.68	−27:46:49.8	30.6 ± 0.8	29.7 ± 0.1	29.4 ± 0.2	29.4 ± 0.2	29.6 ± 0.2	10
UDF12-3853-7519	3:32:38.53	−27:47:51.9	<31.4	29.6 ± 0.1	29.4 ± 0.2	29.4 ± 0.2	29.7 ± 0.3	2,7,10
UDF12-4472-6362	3:32:44.72	−27:46:36.2	30.8 ± 1.0	29.0 ± 0.1	29.4 ± 0.3	28.8 ± 0.1	28.9 ± 0.1	10
UDF12-3983-6189	3:32:39.83	−27:46:18.9	30.0 ± 0.4	29.2 ± 0.1	29.4 ± 0.2	29.7 ± 0.3	29.4 ± 0.1	1,11
UDF12-3736-6245	3:32:37.36	−27:46:24.5	30.6 ± 0.7	29.4 ± 0.1	29.5 ± 0.2	29.5 ± 0.2	29.6 ± 0.2	7,10
UDF12-3456-6493	3:32:34.56	−27:46:49.3	31.4 ± 3.9	29.6 ± 0.1	29.5 ± 0.2	29.3 ± 0.1	29.2 ± 0.1	7,10
UDF12-3859-6521	3:32:38.59	−27:46:52.1	30.4 ± 0.6	29.3 ± 0.1	29.5 ± 0.2	29.9 ± 0.3	29.5 ± 0.2	7,10
UDF12-4384-6311	3:32:43.84	−27:46:31.1	<30.9	29.8 ± 0.2	29.6 ± 0.3	29.5 ± 0.2	29.9 ± 0.4	10
UDF12-3755-6019	3:32:37.55	−27:46:01.9	<31.4	29.9 ± 0.2	29.6 ± 0.2	29.9 ± 0.4	29.6 ± 0.2	7,10
UDF12-3975-7451	3:32:39.75	−27:47:45.1	30.9 ± 1.1	29.4 ± 0.1	29.6 ± 0.2	29.2 ± 0.2	29.3 ± 0.2	7,10
UDF12-4201-7074	3:32:42.01	−27:47:07.4	30.6 ± 1.0	29.6 ± 0.1	29.6 ± 0.2	30.0 ± 0.4	29.6 ± 0.2	10
UDF12-4037-6560	3:32:40.37	−27:46:56.0	<31.3	29.9 ± 0.2	29.6 ± 0.2	30.1 ± 0.4	30.1 ± 0.3	7,10
UDF12-4426-6367	3:32:44.26	−27:46:36.7	30.8 ± 1.4	29.6 ± 0.1	29.6 ± 0.3	29.7 ± 0.3	29.5 ± 0.2	...
UDF12-3909-6092	3:32:39.09	−27:46:09.2	30.2 ± 0.6	29.5 ± 0.1	29.7 ± 0.2	30.3 ± 0.4	29.9 ± 0.3	10
UDF12-4143-7041	3:32:41.43	−27:47:04.1	30.6 ± 0.7	29.9 ± 0.2	29.8 ± 0.2	30.2 ± 0.4	30.0 ± 0.4	10
UDF12-3696-5536	3:32:36.96	−27:45:53.6	30.5 ± 0.5	29.7 ± 0.2	29.8 ± 0.3	29.3 ± 0.2	29.9 ± 0.3	7,10
UDF12-3897-8116	3:32:38.97	−27:48:11.6	30.7 ± 0.8	29.9 ± 0.2	29.8 ± 0.3	30.0 ± 0.4	29.8 ± 0.3	10
UDF12-4288-6261	3:32:42.88	−27:46:26.1	30.7 ± 1.0	29.7 ± 0.2	29.8 ± 0.2	30.0 ± 0.3	30.5 ± 0.7	10
UDF12-3817-7327	3:32:38.17	−27:47:32.7	<30.5	30.0 ± 0.2	29.8 ± 0.3	30.0 ± 0.4	30.3 ± 0.6	11
UDF12-4379-6510	3:32:43.79	−27:46:51.0	30.8 ± 1.2	29.4 ± 0.1	29.9 ± 0.3	29.8 ± 0.3	29.8 ± 0.3	10
UDF12-3691-6517	3:32:36.91	−27:46:51.7	<30.7	30.0 ± 0.2	29.9 ± 0.3	29.7 ± 0.3	30.2 ± 0.4	8,10
UDF12-4071-7347	3:32:40.71	−27:47:34.7	<31.4	29.7 ± 0.2	30.0 ± 0.4	29.4 ± 0.2	30.0 ± 0.6	7,10
UDF12-4036-8022	3:32:40.36	−27:48:02.2	<31.2	30.1 ± 0.2	30.0 ± 0.4	29.9 ± 0.3	30.7 ± 1.3	3,7,10
UDF12-3922-6149	3:32:39.22	−27:46:14.9	30.8 ± 1.0	30.0 ± 0.2	30.2 ± 0.5	30.6 ± 0.6	30.1 ± 0.3	10
UDF12-4245-6534	3:32:42.45	−27:46:53.4	<30.9	30.3 ± 0.2	30.2 ± 0.4	29.5 ± 0.2	29.6 ± 0.2	11
UDF12-4263-6416	3:32:42.63	−27:46:41.6	31.1 ± 3.2	30.0 ± 0.2	30.2 ± 0.3	30.3 ± 0.5	30.1 ± 0.4	10
UDF12-4090-6084	3:32:40.90	−27:46:08.4	<31.3	30.2 ± 0.3	30.5 ± 0.6	30.3 ± 0.4	29.8 ± 0.3	11
UDF12-4019-6190	3:32:40.19	−27:46:19.0	<31.0	29.9 ± 0.2	30.5 ± 0.6	29.9 ± 0.3	29.8 ± 0.2	10

Notes. z-drop photometry. All magnitudes listed are measured in the 70% inclusive aperture sizes listed in Section 2.4 and not corrected to total here. We also note that errors in magnitude space become significantly asymmetric below $\sim 10\sigma$. We have plotted the larger error wherever appropriate. Upper limits are 1σ.
[a] Photometric errors <10%.
References. (1) McLure et al. 2010; (2) Oesch et al. 2010; (3) Finkelstein et al. 2010; (4) Wilkins et al. 2011a; (5) Yan et al. 2010; (6) Lorenzoni et al. 2011; (7) Bouwens et al. 2011; (8) Bouwens et al. 2011 potential; (9) McLure et al. 2011; (10) McLure et al. 2013 robust; (11) McLure et al. 2013 potential.

4. THE LUMINOSITY FUNCTION AT $z \sim 7$ AND $\sim$8 FROM UDF12 DATA

With our candidate selection completed, we now turn to evaluating the $z \simeq 7$ and 8 luminosity functions. The key issue in converting numbers of sources of known absolute magnitude into a comoving density of luminosities is, of course, the redshift-dependent selection function which defines the visibility as a function of apparent magnitude as well as the optimum algorithm for fitting a function to the resulting number density. We now introduce the algorithms we will utilize for both of these critical steps.

4.1. Simulations

We first describe how we calculate the selection function used to determine the effective volumes for our luminosity function calculations.

To create synthetic fluxes for galaxies in our simulations, we assume an input UV slope $\beta = -2.0$. This choice is motivated by the results of Dunlop et al. (2013), who find no conclusive evidence for an intrinsic scatter in β from this value at $z \sim 7$–8 in the UDF12 field (cf. Wilkins et al. 2011b; Bouwens et al. 2012b; Finkelstein et al. 2012). We also assume that these galaxies display no Lyα in emission, motivated by the rarity of detectable

Table 3
Y-drops $7.3 < z < 8.5$

ID	R.A.	Decl.	Y_{105W}	J_{125W}	J_{140W}	H_{160W}	References
UDF12-3880-7072	3:32:38.80	−27:47:07.2	28.0 ± 0.1[a]	27.3 ± 0.1[a]	27.3 ± 0.1[a]	27.2 ± 0.1[a]	1,2,3,4,5,7,9,10
UDF12-4470-6443	3:32:44.70	−27:46:44.3	28.5 ± 0.1	27.8 ± 0.1[a]	27.8 ± 0.1[a]	27.8 ± 0.1[a]	1,2,3,5,7,9,10
UDF12-3952-7174	3:32:39.52	−27:47:17.4	29.3 ± 0.1	28.3 ± 0.1	28.2 ± 0.1	28.0 ± 0.1	1,2,3,5,7,9,10
UDF12-4314-6285	3:32:43.14	−27:46:28.5	29.0 ± 0.1	28.3 ± 0.1	28.2 ± 0.1	28.1 ± 0.1[a]	1,2,3,4,5,7,9,11
UDF12-3722-8061	3:32:37.22	−27:48:06.1	29.0 ± 0.1	28.3 ± 0.1	28.3 ± 0.1	28.3 ± 0.1	1,2,3,5,7,9,10
UDF12-3813-5540	3:32:38.13	−27:45:54.0	30.1 ± 0.2	28.6 ± 0.1	28.5 ± 0.1	28.4 ± 0.1	1,3,5,6,7,9,10
UDF12-3780-6001	3:32:37.80	−27:46:00.1	29.8 ± 0.2	28.6 ± 0.1	28.6 ± 0.1	28.7 ± 0.1	1,3,5,6,7,10
UDF12-3764-6015	3:32:37.64	−27:46:01.5	30.5 ± 0.3	28.9 ± 0.1	28.9 ± 0.1	28.8 ± 0.1	1,3,5,7,10
UDF12-3939-7040	3:32:39.39	−27:47:04.0	30.0 ± 0.2	29.1 ± 0.1	29.1 ± 0.1	28.9 ± 0.1	10
UDF12-4474-6450	3:32:44.74	−27:46:45.0	29.7 ± 0.2	29.0 ± 0.1	29.1 ± 0.2	29.1 ± 0.1	1,2,3,5,7,10
UDF12-4309-6277	3:32:43.09	−27:46:27.7	30.3 ± 0.3	28.9 ± 0.1	29.4 ± 0.2	29.3 ± 0.1	1,3,5,7,11
UDF12-4309-6260	3:32:43.09	−27:46:26.0	30.1 ± 0.2	29.3 ± 0.2	28.9 ± 0.1	29.3 ± 0.2	7,10
UDF12-3463-6472	3:32:34.63	−27:46:47.2	30.3 ± 0.2	29.6 ± 0.2	29.3 ± 0.2	29.4 ± 0.2	7
UDF12-3551-7443	3:32:35.51	−27:47:44.3	30.7 ± 0.4	29.5 ± 0.2	29.9 ± 0.4	29.4 ± 0.3	7,11
UDF12-4336-6203	3:32:43.36	−27:46:20.3	<31.8	29.5 ± 0.2	29.6 ± 0.2	29.4 ± 0.2	...
UDF12-4240-6550	3:32:42.40	−27:46:55.0	30.4 ± 0.3	29.4 ± 0.1	29.7 ± 0.2	29.5 ± 0.2	7,10
UDF12-4033-8026	3:32:40.33	−27:48:02.6	30.1 ± 0.3	29.3 ± 0.2	29.6 ± 0.3	29.5 ± 0.3	3,7,10
UDF12-4308-6242	3:32:43.08	−27:46:24.2	30.4 ± 0.3	29.7 ± 0.3	30.0 ± 0.4	29.6 ± 0.2	7,10
UDF12-3931-6180	3:32:39.31	−27:46:18.0	29.8 ± 0.2	29.3 ± 0.2	29.3 ± 0.1	29.6 ± 0.2	10
UDF12-3934-7256	3:32:39.34	−27:47:25.6	31.2 ± 0.7	29.8 ± 0.3	30.0 ± 0.3	29.7 ± 0.2	7,11
UDF12-3881-6343	3:32:38.81	−27:46:34.3	30.6 ± 0.4	29.9 ± 0.4	30.0 ± 0.4	29.8 ± 0.3	11
UDF12-3681-6421	3:32:36.81	−27:46:42.1	<31.4	30.0 ± 0.4	30.0 ± 0.4	29.8 ± 0.3	7,11
UDF12-4294-6560	3:32:42.94	−27:46:56.0	30.8 ± 0.6	29.9 ± 0.3	30.5 ± 0.7	29.9 ± 0.3	11
UDF12-3920-6322	3:32:39.20	−27:46:32.2	<31.9	29.9 ± 0.3	29.7 ± 0.3	29.9 ± 0.3	10
UDF12-3858-6150	3:32:38.58	−27:46:15.0	30.3 ± 0.3	29.8 ± 0.3	30.3 ± 0.4	29.9 ± 0.3	11
UDF12-4344-6547	3:32:43.44	−27:46:54.7	<31.9	30.0 ± 0.3	30.1 ± 0.4	30.0 ± 0.3	10
UDF12-4101-7216	3:32:41.01	−27:47:21.6	30.4 ± 0.2	29.9 ± 0.3	30.0 ± 0.3	30.9 ± 0.8	10

Notes. *Y*-drop photometry. All magnitudes listed are measured in the 70% inclusive aperture sizes listed in Section 2.4 and not corrected to total here. We also note that errors in magnitude space become significantly asymmetric below $\sim 10\sigma$. We have plotted the larger error wherever appropriate. Upper limits are 1σ.
[a] Photometric errors <10%.
References. (1) McLure et al. 2010; (2) Oesch et al. 2010; (3) Finkelstein et al. 2010; (4) Wilkins et al. 2011a; (5) Yan et al. 2010; (6) Lorenzoni et al. 2011; (7) Bouwens et al. 2011; (8) Bouwens et al. 2011 potential; (9) McLure et al. 2011; (10) McLure et al. 2013 robust; (11) McLure et al. 2013 potential.

emission in recent studies (e.g., Pentericci et al. 2011; Schenker et al. 2012; Ono et al. 2012). Fluxes are computed by applying intergalactic extinction from Meiksin (2006) to a Bruzual & Charlot (2003) synthetic spectrum consistent with this value of β.

We parameterize our selection efficiency, $S(m, z)$, as a function of redshift and the magnitude for the filter (or filters for the UDF12 data) used to determine the rest-frame UV magnitude. In each field, we determine the shape of the selection function first using numerical simulations only, which take into account the limiting magnitudes in each filter for point sources. In steps of 0.01 in redshift and 0.05 in magnitude, we take the synthetic flux from our galaxy model, perturb it by the appropriate noise, and apply our color–color selection criteria. At each step of z, m, and for each field, we perform this $N = 1000$ times to construct a complete surface for our selection function. We define the selection function produced by this process as $S_{\rm numeric}(m, z)$.

However, this selection function is only appropriate if these galaxies are point sources in otherwise blank fields, which is certainly not the case. The marginally resolved nature of our targets will result in higher incompleteness levels at faint magnitudes than for point sources. It is imperative to correct for this effect, as a varying completeness correction can produce large differences in the faint end slope (Grazian et al. 2012). To account for this incompleteness, as well as that caused by area in the images obscured by brighter sources, we rely on inserting synthetic galaxy images into our mosaics for each field. We generate a synthetic template with a Sérsic index of 1.5, consistent with a stack of Lyman break galaxies (LBGs) at $z \sim 4$ (Oesch et al. 2010). The template image has a half-light radius of 0.35 kpc, motivated by the results of Ono et al. (2013), who perform a detailed measurement of the sizes of UDF12 high-redshift candidates. This template is then convolved with the PSF for each filter, multiplied by the appropriate model flux as described above, and inserted into the image in a random location. After inserting $N = 1000$ non-overlapping sources, we run the SExtractor program for object detection and compute fluxes and errors in the same manner as for our science images. We perform this simulation at the peak of each of our selection functions in redshift space, in steps of 0.05 in magnitude. This peak efficiency at a given magnitude $\epsilon(m)$ is then used to normalize our selection function such that our total selection function used to compute effective volumes is given by $S_{\rm total}(m, z) = S_{\rm numeric}(m, z) \times \epsilon(m)$. The final selection functions for both z-drops and Y-drops in the UDF are presented in Figure 2.

4.2. Maximum Likelihood Luminosity Functions

Using the new UDF12 data and previous observations, we assemble dropout samples at $z \sim 7$ and ~ 8 in multiple fields. For each sample, we split the galaxy number counts into bins of width $\Delta M = 0.5$ in absolute magnitude $M_{\rm UV}$. We use these binned galaxy number counts and our simulations of photometric scattering and low-redshift contaminants to determine the high-redshift stepwise maximum likelihood (SWML;

Table 4
SWML Determination of the $z \sim 7$ LF

M_{UV}	$\log \phi_k$ (Mpc^{-3} mag^{-1})
−20.65	$-4.29^{+0.29}_{-0.28}$
−20.15	$-3.71^{+0.14}_{-0.10}$
−19.65	$-3.31^{+0.08}_{-0.10}$
−19.15	$-3.02^{+0.13}_{-0.06}$
−18.65	$-2.98^{+0.17}_{-0.23}$
−18.15	$-2.56^{+0.19}_{-0.06}$
−17.65	$-2.23^{+0.12}_{-0.09}$
−17.15	$-3.03^{+0.54}_{-2.34}$

Table 5
SWML Determination of the $z \sim 8$ LF

M_{UV}	$\log \phi_k$ (Mpc^{-3} mag^{-1})
−22.00	<5.01
−21.50	$-5.02^{+0.44}_{-0.47}$
−21.00	$-4.28^{+0.16}_{-0.24}$
−20.50	$-4.15^{+0.12}_{-0.43}$
−20.00	$-3.54^{+0.17}_{-0.06}$
−19.50	$-3.34^{+0.15}_{-0.17}$
−19.00	$-2.97^{+0.09}_{-0.20}$
−18.50	$-2.91^{+0.14}_{-0.24}$
−18.00	$-2.61^{+0.18}_{-0.20}$
−17.50	$-2.57^{+0.25}_{-0.74}$

Efstathiou et al. 1988) and Schechter (1976) galaxy luminosity functions $\Phi(M_{UV})$ in units of Mpc^{-3} mag^{-1}.

4.2.1. Stepwise Maximum Likelihood Luminosity Function

The SWML luminosity function aims to jointly fit the binned galaxy abundance Φ_k in the k^{th} of N_{bin} magnitude bins. For each bin, the maximum likelihood values for Φ_k are determined by using the observed number of galaxies $n_{obs,k}$, the effective volume $V_{eff,k}$ for galaxies with intrinsic M_{UV} in the bin, and the probabilities $P_{i,j}$ for scattering galaxies with intrinsic M_{UV} in bin i into bin j owing to photometric noise, and the number of low-redshift contaminants $n_{con,k}$ for the bin calculated as described in Section 4.1. Given Φ_k, we construct the expected number of galaxies in each bin as

$$n_{exp,k} = \Phi_k V_{eff,k} \left(1 - \sum_{i \neq k} P_{k,i}\right) + \sum_{i \neq k} \Phi_i V_{eff,i} P_{i,k} + n_{con,k}, \quad (5)$$

where the summations run over N_{bin}. In practice, when using a bin width $\Delta M_{UV} = 0.5$, galaxies do not scatter by more than one bin and the summations are trivial. We account for photometric scattering of sources into our faintest bin by a simple extrapolation of the luminosity function to yet fainter magnitudes.

To fit the shape of our SWML, we can use the likelihood of observing $n_{obs,k}$ given the expected number $n_{exp,k}$:

$$p(n_{obs,k}|n_{exp,k}) = \left(\frac{n_{exp,k}}{\Sigma_j n_{exp,j}}\right)^{n_{obs,k}}. \quad (6)$$

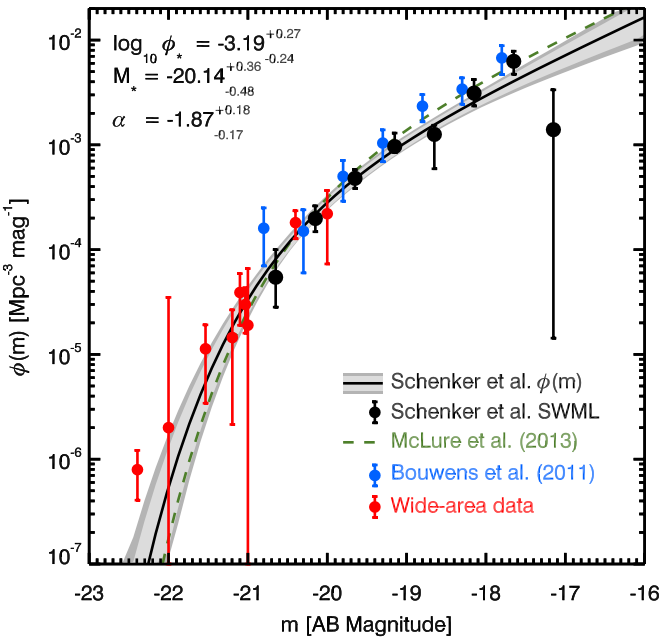

Figure 4. The luminosity function of star-forming galaxies at $z \sim 7$ from the z_{850}-drop sample. The black points were determined using the UDF12 data set and other *HST* data mentioned in this work. The red points denote wide-area ground based data increase the range in luminosity. The black line defines the maximum likelihood Schechter luminosity function and the shaded light gray region denotes the 68% confidence interval. The shaded dark gray region denotes the 68% confidence interval when errors from cosmic variance are included. The green dashed line denotes the fit of McLure et al. (2013).

(A color version of this figure is available in the online journal.)

The SWML luminosity function Φ_k is determined by maximizing the product of these individual likelihoods across all bins and across all fields. Photometric scatter correlates the individual Φ_k for each field, and the SWML values must therefore be determined simultaneously. This calculation amounts to an N_{bin}-parameter estimation problem, and we use the *MultiNest* nested sampling code for Bayesian inference problems (Feroz & Hobson 2008; Feroz et al. 2009) to maximize the Φ_k likelihoods.

To fit the overall normalization of our SWML, we sum $n_{obs,k}$ across all fields for each magnitude bin. Since we expect this quantity to be Poisson distributed, we can easily generate a posterior distribution of the normalization for each bin. To find our final posterior distribution, for the normalization we multiply the posteriors generated in this manner across all bins.

The results of the SWML luminosity function calculation for redshift $z \sim 7$ is shown in Figure 4 and for redshift $z \sim 8$ in Figure 5. The data points indicate the maximum likelihood Φ_k at each magnitude for our sample taking into account all fields, while error bars indicate the smallest marginalized interval to encompass 68% of the likelihood for each bin. We list the tabulated SWML data points and error for redshift $z \sim 7(8)$ in Table 4(5).

4.2.2. Schechter Luminosity Functions

A determination of the Schechter (1976) luminosity function parameters is calculated by estimating the mean galaxy abundance in each bin as

$$\Phi_k = \frac{1}{\Delta M_{UV}} \int_{M_{UV,k}-0.5\Delta M_{UV}}^{M_{UV,k}+0.5\Delta M_{UV}} \Phi(M) dM \quad (7)$$

and then using Equations (5) and (6) to calculate the likelihood of the fit parameters. The likelihoods of each binned sample in

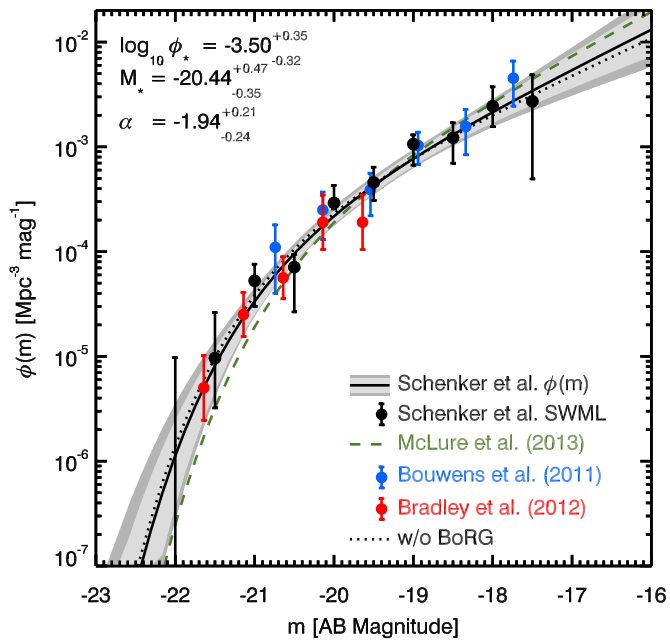

Figure 5. The luminosity function of star-forming galaxies at $z \sim 8$ from the Y_{105}-drop sample. The black points were determined using the UDF12 data set and other *HST* data mentioned in this work. The red points denote data from the Bradley et al. (2012) analysis of the BoRG fields that increase the range in luminosity. The black line defines the maximum likelihood Schechter luminosity function and the shaded light gray region denotes the 68% confidence interval The shaded dark gray region includes the error contribution from cosmic variance. The green line denotes our fit when removing the BoRG data points; we note that our fit to the faint end slope is remarkably insensitive to their inclusion/exclusion. The green dashed line denotes the fit of McLure et al. (2013).

(A color version of this figure is available in the online journal.)

each field are multiplied. To improve constraints at the bright end at $z \sim 7$, when fitting we also include data from the ground-based surveys of Ouchi et al. (2009), Castellano et al. (2010), and Bowler et al. (2012). Incorporating the wide-area ground-based constraints is critical as even our wide-area *HST* data only detects sources dimmer than $M_{\rm UV} \sim -21.0$, or approximately 1 mag brighter than $M^*_{\rm UV}$ at this redshift. As pointed out in Robertson (2010a), Bouwens et al. (2011), and Bradley et al. (2012), there remains a large degeneracy between $M^*_{\rm UV}$ and the faint end slope, α, without sufficient data at the bright end. These additional data are incorporated using the published data points and errors through a χ^2 likelihood, assuming the reported errors are Gaussian. The maximum likelihood Schechter function parameters are determined using *MultiNest* to conduct Bayesian inference.

The Schechter function fit results for redshift $z \sim 7$ are shown in Figure 4 and for $z \sim 8$ in Figure 5, with the maximum likelihood models shown as a black line. At $z \sim 7$, the best fit Schechter function parameters are $\log_{10}\phi_\star = -3.19^{+0.27}_{-0.24}\,\log_{10}{\rm Mpc}^{-3}\,{\rm mag}^{-1}$, $M_{{\rm UV},\star} = -20.14 \pm 0.4$, and $\alpha_{z\sim7} = -1.87^{+0.18}_{-0.17}$. The uncertainty range for each parameter reflects the smallest interval in each marginalized distribution to encompass 68% of the posterior probability. At $z \sim 8$, the best fit Schechter function parameters are $\log_{10}\phi_\star = -3.50^{+0.35}_{-0.32}\,\log_{10}{\rm Mpc}^{-3}\,{\rm mag}^{-1}$, $M_{{\rm UV},\star} = -20.44^{+0.5}_{-0.4}$, and $\alpha_{z\sim8} = -1.94^{+0.21}_{-0.24}$. In Figures 4 and 5, the light gray shaded regions denote the inner 68% of the marginalized posterior distribution in galaxy abundance at each magnitude. The dark gray regions in each plot represent the 68% marginalized confidence intervals including potential error contributions from cosmic variance, discussed in Section 4.2.3.

At $z \sim 8$, we also include a Schechter function fit excluding the Bradley et al. (2012) BoRG data, denoted by the dotted black line. The best fit parameters are $\log_{10}\phi_\star = -3.47 \pm 0.39$, $\log_{10}{\rm Mpc}^{-3}\,{\rm mag}^{-1}$, $M_{{\rm UV},\star} = -20.45 \pm 0.50$, and $\alpha_{z\sim8} = -1.87 \pm 0.25$. This results in nearly identical values for $\phi_\star$ and $M_{{\rm UV},\star}$, with a slightly shallower faint end slope and marginally larger error bars compared to the fit with the data included. Thus, even without the wide-area data, we still find strong evidence for a steep value of α.

We caution the reader against an over-interpretation of the faintest bins in our Luminosity functions. Although heating of the intergalactic medium during reionization is expected to suppress the formation of dwarf galaxies below a characteristic halo mass (e.g., Wyithe & Loeb 2006; Muñoz & Loeb 2011), the density determinations of ϕ_k in our faintest bins are very sensitive both to upscattering of sources below the limit and completeness corrections. This is largely a result of being in a regime where the effective volume is rapidly changing as a function of magnitude. For example, simply dividing the number of observed sources, after correcting for the expected contamination, in our faintest $z \sim 7$ bin by the effective volume yields $\log_{10}\phi_k \sim -2.3$, which is much more in line with our best fit Schechter function parameters. Though we have made our best effort to quantify and account for corrections arising from finite size, scattering, and contamination, the situation remains difficult at the faintest reaches of the survey.

4.2.3. Cosmic Variance

Although we have not included the effects of cosmic variance in any of the parameter estimates given above, it nonetheless is useful to obtain some indication of its effect. To first order, cosmic variance is unlikely to have a major effect on one of the primary goals of this paper, namely an estimate of the faint end slope at $z \sim 7$–8. In the following, we therefore give an approximate calculation of the effective variance arising from large scale structure.

Density fluctuations owing to large scale modes can cause variations in the observed galaxy abundance beyond uncertainties arising from number counting statistics. Following Robertson (2010a), by using our best fit luminosity functions at $z \sim 7$–8, we can characterize these cosmic variance uncertainties for each field in our sample. We use the linear power spectrum calculated with the Eisenstein & Hu (1998) transfer function, conservatively assuming root-mean-squared density fluctuations in volumes of radius $8\,h^{-1}$ Mpc of $\sigma_8 = 0.9$ at $z = 0$, to estimate the typical root-mean-squared density fluctuations in our survey fields at the redshifts of interest. To estimate the clustering bias of galaxies at these redshifts, we simply match the abundance of galaxies from our luminosity functions with the abundance of dark matter halos provided by the Tinker et al. (2008) halo mass function, and then assign the clustering bias of the halos to the galaxies assuming the bias function of Tinker et al. (2010). For the UDF, to our limiting magnitude we find that the typical cosmic variance (the fractional uncertainty in the total galaxy number counts owing to large scale structure) is $\sigma_{\rm CV} \approx 0.30$ at $z \sim 7$ and $\sigma_{\rm CV} \approx 0.36$ at $z \sim 8$. The typical bias for galaxies in the UDF is $b \approx 5.0$ at $z \sim 7$ and $b \approx 6.2$ at $z \sim 8$. For UDF-P1, we find that the typical cosmic variance is $\sigma_{\rm CV} \approx 0.33$ at $z \sim 7$ and $\sigma_{\rm CV} \approx 0.38$ at $z \sim 8$. The typical bias for galaxies in the UDF-P1 is $b \approx 5.4$ at $z \sim 7$ and $b \approx 6.6$ at $z \sim 8$. For UDF-P2, we find that the typical cosmic variance is

$\sigma_{\rm CV} \approx 0.32$ at $z \sim 7$ and $\sigma_{\rm CV} \approx 0.37$ at $z \sim 8$. The typical bias for galaxies in the UDF-P2 is $b \approx 5.2$ at $z \sim 7$ and $b \approx 6.5$ at $z \sim 8$. For ERS, we find that the typical cosmic variance is $\sigma_{\rm CV} \approx 0.30$ at $z \sim 7$ and $\sigma_{\rm CV} \approx 0.34$ at $z \sim 8$. The typical bias for galaxies in the ERS field is $b \approx 6.4$ at $z \sim 7$ and $b \approx 7.7$ at $z \sim 8$. Lastly, for CANDELS-Deep we find that the typical cosmic variance is $\sigma_{\rm CV} \approx 0.26$ at $z \sim 7$ and $\sigma_{\rm CV} \approx 0.30$ at $z \sim 8$. The typical bias for galaxies in CANDELS-Deep is $b \approx 6.3$ at $z \sim 7$ and $b \approx 7.6$ at $z \sim 8$.

We also make an attempt to model the additional uncertainties introduced to our luminosity function calculations by cosmic variance. We repeat the calculations of Sections 4.2.1 and 4.2.2, but modified to marginalize over fluctuations in the galaxy abundance in our survey volumes owing to density fluctuations. We calculate the expected number counts $n_{{\rm exp},k}$ as before (Equation (5)), but for the likelihood of observing $n_{{\rm obs},k}$ galaxies given $n_{{\rm exp},k}$, we use

$$p(n_{{\rm obs},k}|n_{{\rm exp},k}, \sigma_{\rm CV}) = \int_{-1}^{\infty} d\delta_g \, p_{\rm LN}(\delta_g|\sigma_{\rm CV}) \left(\frac{(1+\delta_g) n_{{\rm exp},k}}{\sum_j n_{{\rm exp},j}} \right)^{n_{{\rm obs},k}}, \quad (8)$$

where $\sigma_{\rm CV}$ is the cosmic variance uncertainty in the number counts and the distribution of galaxy count overdensities δ_g is modeled as a lognormal

$$p_{\rm LN}(\delta_g|\sigma_{\rm CV}) = \frac{1}{\sqrt{2\pi x^2}} \exp\left[-\frac{1}{2} \left(\frac{y}{x} + \frac{x}{2} \right)^2 \right], \quad (9)$$

with $y \equiv \ln(1+\delta_g)$ and $x \equiv [\ln(1+\sigma_{\rm CV}^2)]^{1/2}$. We have adopted this model from Robertson (2010b, see also Adelberger et al. 1998), who used the lognormal distribution to model galaxy count fluctuations in the quasi-linear regime. Note that in the limit $\sigma_{\rm CV} \to 0$, we recover the previous method, and this approach treats the possible galaxy count fluctuations of each field independently. Given the cosmic variance uncertainty estimates calculated above, we conservatively adopt $\sigma_{\rm CV}(z \sim 7) = 0.4$ and $\sigma_{\rm CV}(z \sim 8) = 0.45$. Since Equation (8) models the shape of the luminosity function, we adopt the same normalization constraint as before, treating contributions to the total galaxy count from all fields simultaneously.

The results for such an extension of the fitting are shown in Figures 4 and 5 as dark gray bands (68% confidence intervals including cosmic variance uncertainty). Including cosmic variance uncertainty and using the likelihood in Equation (8), we find best fit Schechter function parameters of $\log_{10}\phi_\star = -3.18^{+0.32}_{-0.38}$, $M_{{\rm UV},\star} = -20.14^{+0.41}_{-0.46}$, and $\alpha_{z\sim7} = -1.87^{+0.25}_{-0.22}$ at redshift $z \sim 7$ and $\log_{10}\phi_\star = -3.52^{+0.42}_{-0.58}$, $M_{{\rm UV},\star} = -20.47^{+0.52}_{-0.75}$, and $\alpha_{z\sim8} = -1.94^{+0.34}_{-0.30}$ at redshift $z \sim 8$. The fitting method recovers almost exactly the best fit parameters found without accounting for cosmic variance uncertainty, but the marginalized uncertainties on the parameters increase. The uncertainties on the faint-end slope α increase by $\Delta\sigma_\alpha \approx 0.05$–$0.08$ at redshift $z \sim 7$ and by $\Delta\sigma_\alpha \approx 0.09$–$0.10$. Since we have assumed a conservatively large cosmic variance uncertainty, we expect these additional uncertainties to be somewhat overestimated. Nonetheless, these observations have provided high precision measures of the luminosity function parameters at $z \sim 7$ and $z \sim 8$, even accounting for cosmic variance uncertainties.

5. DISCUSSION

5.1. Comparison with McLure et al. (2013)

We now compare our results with those of McLure et al. (2013). Of our combined sample of 74 UDF12 sources, 57 are identified as robust and 13 as non-robust, leaving only 4 not selected in either category by McLure et al. (2013). Examining these objects individually, one was excluded as it was too close to the edge of the detector, although this difference is accounted for in the selection volume simulations for each paper. The remaining three objects were excluded by virtue of a concern by McLure et al. (2013) that they might lie at $z < 6.5$. The SED approach imposes a strict lower redshift limit, whereas our dropout selection functions maintain some sensitivity to $z \sim 6.0$–6.3 (Figure 2). These differences in selection sensitivity are fully accounted for in the two analyses.

Notwithstanding the agreement, McLure et al. (2013) has amassed a sample of 100 robust high-redshift candidates in comparison to our 74. We list here the reasons a number of these objects were excluded from our sample. Two objects lie at $z \geqslant 9.5$, which our selection criteria are insensitive to. Our more stringent optical rejection criteria preclude another seven candidates from our final sample. Additionally, we exercised caution in excluding an additional two candidates which lie in close proximity to extended, low-redshift galaxies. When the above differences are accounted for, we find that McLure et al. (2013) includes an additional 28 $z > 6.5$ candidates that are not accepted by our selection functions, which only target objects with evidence of a firm spectral break in adjacent filters.

As expected therefore, the results of the luminosity function studies are in excellent agreement. The best fit parameters for both studies are summarized in Table 6. All derived parameters are consistent within 1σ with error bars of comparable size. In particular, the faint end slopes, α, agree to well within the 1σ errors. As one of the main goals of UDF12 was to improve this measurement, the robustness of our conclusions with respect to differing selection methodology is reassuring.

5.2. Comparison with Other High-redshift Literature

It is instructive to compare the Schechter function parameters derived by our study to those of previous analyses, both at these redshifts and below. While the full array of derived parameters from recent high-redshift studies is available in Table 6, we focus here again on the faint end slope, α. Previous studies at redshifts $2 < z < 6$ find a remarkably consistent value of $\alpha \sim -1.7$ across this range (e.g., Oesch et al. 2007; Bouwens et al. 2007; Reddy & Steidel 2009; McLure et al. 2009).

At the moderately larger redshift of $z \sim 7$, the situation remains much more uncertain. While Bouwens et al. (2011) claim a significantly steepened value of $\alpha = -2.01 \pm 0.21$, at $z \sim 7$ Grazian et al. (2012) find no signal of slope evolution, determining $\alpha = -1.7 \pm 0.1$. Our determination of $\alpha_{z\sim7} = -1.87^{+0.18}_{-0.17}$, though still consistent with -1.7, does suggest a steepening of the faint end slope with increasing redshift, especially when considering the value of $\alpha = -1.90^{+0.14}_{-0.15}$ determined by McLure et al. (2013).

At $z \sim 8$, the existing literature largely agrees on a steepening of α, with the most recent determinations by Bouwens et al. (2011), Oesch et al. (2012), and Bradley et al. (2012) finding values between -1.9 and -2.1. Extending 0.25 mag fainter in UV luminosity than any previous study, our determination of $\alpha_{z\sim8} = -1.94^{+0.21}_{-0.24}$ provides increased support for this

Table 6
Best-fit LF Parameters from Recent Studies

Study	$z \simeq 7$			$z \simeq 8$		
	$\log_{10}\phi_\star$ (Mpc^{-3})	$M_{\rm UV,\star}$	α	$\log_{10}\phi_\star$ (Mpc^{-3})	$M_{\rm UV,\star}$	α
This work	$-3.19^{+0.27}_{-0.24}$	$-20.14^{+0.36}_{-0.48}$	$-1.87^{+0.18}_{-0.17}$	$-3.50^{+0.35}_{-0.32}$	$-20.44^{+0.47}_{-0.35}$	$-1.94^{+0.21}_{-0.24}$
McLure et al. (2013)	$-2.96^{+0.18}_{-0.23}$	$-19.90^{+0.23}_{-0.28}$	$-1.90^{+0.14}_{-0.15}$	$-3.35^{+0.28}_{-0.47}$	$-20.12^{+0.37}_{-0.48}$	$-2.02^{+0.22}_{-0.23}$
Lorenzoni et al. (2013)	-3.14	-20.19	-1.9 (fixed)	-3.02	-19.37	-1.9 (fixed)
Bradley et al. (2012)	...	...	...	$-3.37^{+0.26}_{-0.29}$	$-20.26^{+0.29}_{-0.34}$	$-1.98^{+0.23}_{-0.22}$
Oesch et al. (2012)	...	...	...	$-3.30^{+0.38}_{-0.46}$	$-20.04^{+0.44}_{-0.48}$	$-2.06^{+0.35}_{-0.28}$
Grazian et al. (2012)	-3.13 (fixed)	-20.14 (fixed)	-1.7 ± 0.1	...	...	...
Bouwens et al. (2011)	-3.07 ± 0.26	-20.14 ± 0.26	-2.01 ± 0.21	-3.23 ± 0.43	-20.10 ± 0.52	-1.91 ± 0.32

evolution, in concert with the $\alpha_{z\sim8} = -2.02^{+0.22}_{-0.23}$ found by McLure et al. (2013). As noted by many authors (e.g., Robertson et al. 2010; Bouwens et al. 2012a), this will significantly increase the ability of galaxies to maintain the reionization of the intergalactic medium as intrinsically faint sources become more numerous. This steepening is also predicted by conditional luminosity function methods based on the evolution of the dark matter halo mass function (Trenti et al. 2010; Tacchella et al. 2012). We also note that although our derived values of $\phi_\star$ and $M_{\rm UV,\star}$ favor a decreasing $\phi_\star$ with redshift to account for the evolution of the luminosity function, the errors are still too large to rule out an evolution in the characteristic magnitude instead (or a combination). The reader may also wish to read a significantly more detailed analysis of the impact of our survey on reionization in Robertson et al. (2013).

5.3. Summary

Along with McLure et al. (2013), we have uncovered the most comprehensive and robust sample of sub-luminous high-redshift galaxies to date. At moderate magnitudes, $M_{\rm UV} \leqslant -18.0$, we achieve a more refined sample of dropouts, including an additional 3 (3) z-drops (Y-drops) not previously identified as high redshift sources as a result of our improved photometry. Of greater importance, though, are our advances below this UV magnitude; we discover an additional 14 sources at $z \sim 7$ by virtue of our ultra deep Y_{105} image, as well as an additional 5 sources at $z \sim 8$, indicating the steepness of the faint end slope continues beyond 2 mag below $M_{\rm UV,\star}$ at these redshifts. Additionally, our sample is in excellent agreement with the independent determination from McLure et al. (2013). We note that only two of our sources at $z \sim 7$, as well as two at $z \sim 8$, are not present in their final catalog.

With the upcoming *HST Frontier Fields* observations scheduled to begin in Cycle 21, progress in this regime vital to understanding if and when star-forming galaxies can maintain reionization is sure to continue. We stress the gains made by UDF12 strengthen claims of an increased steepness at the faint end and, along with McLure et al. (2013) provide a self-consistent, robust determination of α at redshifts 7 and 8.

US authors acknowledge financial support from the Space Telescope Science Institute under award HST-GO-12498.01-A. J.S.D. acknowledges support of the European Research Council and the Royal Society. R.J.M. acknowledges funding from the Leverhulme Trust. S.C. acknowledges the support of the European Commission through the Marie Curie Initial Training Network ELIXIR. This work is based on data from the *Hubble Space Telescope* operated by NASA through the Space Telescope Science Institute via the association of Universities for Research in Astronomy, Inc. under contract NAS5-26555.

REFERENCES

Adelberger, K. L., Steidel, C. C., Giavalisco, M., et al. 1998, ApJ, 505, 18
Atek, H., Siana, B., Scarlata, C., et al. 2011, ApJ, 743, 121
Beckwith, S. V. W., Stiavelli, M., Koekemoer, A. M., et al. 2006, AJ, 132, 1729
Bertin, E., Mellier, Y., Radovich, M., et al. 2002, in ASP Conf. Ser. 281, Astronomical Data Analysis Software and Systems XI, ed. D. A. Bohlender, D. Durand, & T. H. Handley (San Francisco, CA: ASP), 228
Bouwens, R. J., Illingworth, G. D., Franx, M., & Ford, H. 2007, ApJ, 670, 928
Bouwens, R. J., Illingworth, G. D., Franx, M., & Ford, H. 2008, ApJ, 686, 230
Bouwens, R. J., Illingworth, G. D., Oesch, P. A., et al. 2010, ApJL, 709, L133
Bouwens, R. J., Illingworth, G. D., Oesch, P. A., et al. 2011, ApJ, 737, 90
Bouwens, R. J., Illingworth, G. D., Oesch, P. A., et al. 2012a, ApJL, 752, L5
Bouwens, R. J., Illingworth, G. D., Oesch, P. A., et al. 2012b, ApJ, 754, 83
Bouwens, R. J., Thompson, R. I., Illingworth, G. D., et al. 2004, ApJL, 616, L79
Bowler, R. A. A., Dunlop, J. S., McLure, R. J., et al. 2012, MNRAS, 426, 2772
Bradley, L. D., Trenti, M., Oesch, P. A., et al. 2012, ApJ, 760, 108
Brammer, G. B., van Dokkum, P. G., Illingworth, G. D., et al. 2013, ApJL, 765, L2
Bruzual, G., & Charlot, S. 2003, MNRAS, 344, 1000
Bunker, A. J., Stanway, E. R., Ellis, R. S., & McMahon, R. G. 2004, MNRAS, 345, 374
Bunker, A. J., Wilkins, S., Ellis, R. S., et al. 2010, MNRAS, 409, 55
Casertano, S., de Mello, D., Dickinson, M., et al. 2000, AJ, 120, 2747
Castellano, M., Fontana, A., Paris, D., et al. 2010, A&A, 524, A28
Dunlop, J. S., McLure, R. J., Robertson, B. E., et al. 2012, MNRAS, 420, 901
Dunlop, J. S., Rogers, A. B., McLure, R. J., et al. 2013, MNRAS, in press (arXiv:1212.0860)
Efstathiou, G., Ellis, R. S., & Peterson, B. A. 1988, MNRAS, 232, 431
Eisenstein, D., & Hu, W. 1998, ApJ, 496, 605
Ellis, R. S., McLure, R. J., Dunlop, J. S., et al. 2013, ApJL, 763, L7
Feroz, F., & Hobson, M. P. 2008, MNRAS, 384, 449
Feroz, F., Hobson, M. P., & Bridges, M. 2009, MNRAS, 398, 1601
Finkelstein, S. L., Papovich, C., Giavalisco, M., et al. 2010, ApJ, 719, 1250
Finkelstein, S. L., Papovich, C., Salmon, B., et al. 2012, ApJ, 756, 164
Giavalisco, M., Ferguson, H. C., Koekemoer, A. M., et al. 2004, ApJL, 600, L93
González, V., Labbé, I., Bouwens, R. J., et al. 2010, ApJ, 713, 115
Grazian, A., Castellano, M., Fontana, A., et al. 2012, A&A, 547, 51
Grogin, N. A., Kocevski, D. D., Faber, S. M., et al. 2011, ApJS, 197, 35
Hayes, M., Laporte, N., Pelló, R., Schaerer, D., & Le Borgne, J.-F. 2012, MNRAS, 425, L19
Koekemoer, A. M., Ellis, R. S., McLure, R. J., et al. 2013, ApJS, submitted (arXiv:1212.1448)
Koekemoer, A. M., Faber, S. M., Ferguson, H. C., et al. 2011, ApJS, 197, 36
Koekemoer, A. M., Fruchter, A. S., Hook, R. N., & Hack, W. 2003, in The 2002 HST Calibration Workshop Proceedings: Hubble After the Installation of the ACS and the NICMOS Cooling System, ed. S. Arribas, A. Koekemoer, & B. Whitemore (Baltimore, MD: STScI), 337
Kriek, M., Labbé, I., Conroy, C., et al. 2010, ApJL, 722, L64
Labbé, I., González, V., Bouwens, R. J., et al. 2010, ApJL, 716, L103
Labbe, I., Oesch, P. A., Bouwens, R. J., et al. 2012, arXiv:1209.3037
Landsman, W. B. 1993, in ASP Conf. Ser. 52, Astronomical Data Analysis Software and Systems II, ed. R. J. Hanisch, R. J. V. Brissenden, & J. Barnes (San Francisco, CA: ASP), 246

Lorenzoni, S., Bunker, A. J., Wilkins, S. M., et al. 2011, MNRAS, 414, 1455
Lorenzoni, S., Bunker, A. J., Wilkins, S. M., et al. 2013, MNRAS, 429, 150
Madau, P. 1995, ApJ, 441, 18
McLure, R. J., Cirasuolo, M., Dunlop, J. S., Foucaud, S., & Almaini, O. 2009, MNRAS, 395, 2196
McLure, R. J., Dunlop, J. S., Bowler, R. A. A., et al. 2013, MNRAS, in press arXiv:1212.5222
McLure, R. J., Dunlop, J. S., Cirasuolo, M., et al. 2010, MNRAS, 403, 960
McLure, R. J., Dunlop, J. S., de Ravel, L., et al. 2011, MNRAS, 418, 2074
Meiksin, A. 2006, MNRAS, 365, 807
Muñoz, J. A., & Loeb, A. 2011, ApJ, 729, 99
Oesch, P. A., Bouwens, R. J., Illingworth, G. D., et al. 2010, ApJL, 709, L16
Oesch, P. A., Bouwens, R. J., Illingworth, G. D., et al. 2012, ApJ, 759, 135
Oesch, P. A., Stiavelli, M., Carollo, C. M., et al. 2007, ApJ, 671, 1212
Oke, J. B., & Gunn, J. E. 1983, ApJ, 266, 713
Ono, Y., Ouchi, M., Curtis-Lake, E., et al. 2013, arXiv:1212.3869
Ono, Y., Ouchi, M., Mobasher, B., et al. 2012, ApJ, 744, 83
Ouchi, M., Mobasher, B., Shimasaku, K., et al. 2009, ApJ, 706, 1136
Pentericci, L., Fontana, A., Vanzella, E., et al. 2011, ApJ, 743, 132
Reddy, N. A., & Steidel, C. C. 2009, ApJ, 692, 778
Robertson, B. E. 2010a, ApJ, 713, 1266
Robertson, B. E. 2010b, ApJL, 716, L229
Robertson, B. E., Ellis, R. S., Dunlop, J. S., McLure, R. J., & Stark, D. P. 2010, Natur, 468, 49
Robertson, B. E., Furlanetto, S. R., Schneider, E., et al. 2013, ApJ, 768, 71
Schechter, P. 1976, ApJ, 203, 297
Schenker, M. A., Stark, D. P., Ellis, R. S., et al. 2012, ApJ, 744, 179
Steidel, C. C., Giavalisco, M., Pettini, M., Dickinson, M., & Adelberger, K. L. 1996, ApJL, 462, L17
Tacchella, S., Trenti, M., & Carollo, C. M. 2012, arXiv:1211.2825
Taniguchi, Y., Shioya, Y., & Trump, J. R. 2010, ApJ, 724, 1480
Tinker, J., Kravtsov, A., Klypin, A., et al. 2008, ApJ, 688, 709
Tinker, J., Robertson, B., Kravtsov, A., et al. 2010, ApJ, 724, 878
Trenti, M., Bradley, L. D., Stiavelli, M., et al. 2011, ApJL, 727, L39
Trenti, M., Stiavelli, M., Bouwens, R. J., et al. 2010, ApJL, 714, L202
Wilkins, S. M., Bunker, A. J., Lorenzoni, S., & Caruana, J. 2011a, MNRAS, 411, 23
Wilkins, S. M., Bunker, A. J., Stanway, E., Lorenzoni, S., & Caruana, J. 2011b, MNRAS, 417, 717
Windhorst, R. A., Cohen, S. H., Hathi, N. P., et al. 2011, ApJS, 193, 27
Wyithe, J. S. B., & Loeb, A. 2006, Natur, 441, 322
Yan, H.-J., Windhorst, R. A., Hathi, N. P., et al. 2010, RAA, 10, 867
Yan, H.-J., Yan, L., Zamojski, M. A., et al. 2011, ApJL, 728, L22